EFFECTS OF ELECTRIC POTENTIAL UNCERTAINTY ON ELECTROSTATIC TRACTOR RELATIVE MOTION CONTROL

Julian Hammerl and Hanspeter Schaub

Smead Department of Aerospace Engineering Sciences, University of Colorado Boulder, Boulder, CO, 80303 USA, Email: {julian.hammerl, hanspeter.schaub}@colorado.edu

ABSTRACT

The Electrostatic Tractor (ET) has been proposed to touchlessly remove space debris from geosynchronous orbit (GEO) by taking advantage of inter-craft Coulomb forces. A controlled spacecraft (tug) emits an electron beam onto an uncooperative or retired satellite (debris). Thus, the tug raises its own electrostatic positive potential to 10s of kilovolts, while the debris charges negatively. This results in an attractive force called the electrostatic tractor. Prior research investigated the charged relative motion dynamics and control of the ET for two spherical spacecraft and how charge uncertainty affects the relative motion control stability, but attitude effects could not be studied due to the two-sphere model. This work utilizes the Multi-Sphere Method (MSM) to consider general three-dimensional spacecraft shapes, and investigates how the electric potential uncertainty and debris attitude impact the equilibrium separation distance between the two craft. The results show bounds for safe operations that avoid a collision. State regions are identified where the relative motion is particularly sensitive to potential uncertainty. The relative station keeping performance using either higher or lower fidelity MSM models are compared to demonstrate that even a lower fidelity MSM model can yield good results.

Keywords: active debris removal, touchless, charged astrodynamics, electrostatics.

1. INTRODUCTION

The Geostationary Earth Orbit (GEO) is becoming increasingly populated with both active and retired satellites due to the unique and valuable properties of geosynchronous orbits that allow spacecraft to maintain a fixed position above Earth. In contrast to Low Earth Orbit (LEO), there is no atmospheric drag that eventually deorbits retired satellites and debris. Of the over 1000 geostationary objects, only 340 were controlled as of 2005 [JAH05]. At this time, only one third of the satellites in GEO followed the space debris mitigation guidelines of the Inter-Agency Space Debris Coordination Committee (IADC). These guidelines recommend a minimum altitude increase of at least 235 km after the end of a satellite's mission, depending on spacecraft characteristics such as solar radiation pressure coefficient, cross-sectional area, and mass [Yak05]. The percentage of successful reorbit maneuvers of satellites that reached end-of-life between 2007-2016 increased to 66.1%, but stagnated over the last few years [FL17]. At today's GEO population of over 700 satellites [FL17], this rate of successful maneuvers still leaves over 200 satellites that are either not reorbited to a high enough altitude, or not reorbited at all.

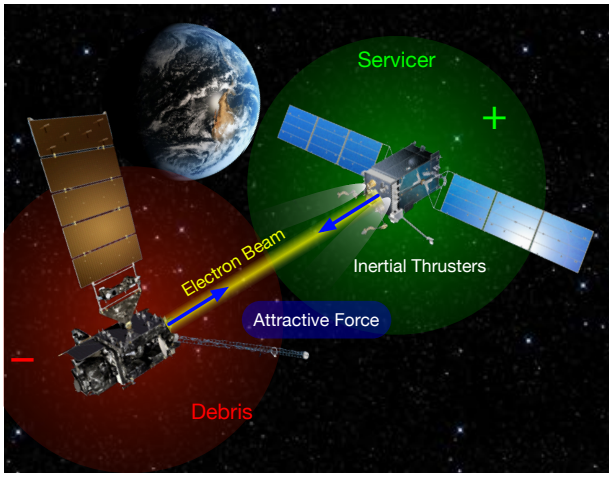

Figure 1: Electrostatic Tractor

Due to the increasing probability of collisions with an increasing number of artificial satellites in Earth orbit [KCP78], Active Debris Removal (ADR) methods are necessary to reduce the number of objects in the geosynchronous belt by relocating dysfunctional satellites to a graveyard orbit several hundred kilometers above GEO. A number of ADR concepts have been investigated for large objects [SGG16, MK19], such as nets [SGG17], harpoons [DTB15], robotic arms [NKO+09] and the Ion Beam Shephard [BP11]. However, most of these concepts involve physical contact between the servicing satellite and the debris object. Nets and harpoons might create new fragments when they impact the de-

bris, and the required tether between the debris and the servicer adds complexity to the removal process. The capture with robotic arms or tentacles requires complicated rendezvous and docking maneuvers. Retired satellites may tumble at rates of 10s of degrees per second [ŠPHS18, PKM09], exceeding the capabilities of certain grappling methods [NK11]. Thus, touchless ADR techniques provide a great benefit for space debris removal.

Similar to the concept of deflecting near Earth asteroids using electrostatic interaction [MIB+08], the Electrostatic Tractor (ET) has been proposed to touchlessly remove space debris from GEO by taking advantage of inter-craft Coulomb forces (Figure 1) [SM12]. A controlled spacecraft, referred to as a servicer or a tug, emits an electron beam onto an uncooperative or retired satellite (debris). The emission of electrons raises the electric potential of the servicer to 10s of kilovolts, while the debris charges negatively due to the bombardment with electrons. Using inertial thrusters, the resulting attractive Coulomb force in the order of milli-Newtons is utilized to relocate the debris to a graveyard orbit without any physical contact. It has been demonstrated that this concept can be used to raise the altitude of a retired satellite by 300 km within two months [HS13], and that it is also possible to touchlessly detumble such satellites [SS13a, BS15, AS19]. The pushing configuration, where the sign of the electric charge is the same for both spacecraft, and the effects of attitude on the relative motion have also been investigated [Asl17, AY18].

One important characteristic of charging in the space environment is the Debye length, which describes how far the electrostatic effects of an object are perceivable. In the cold and dense LEO environment, the Debye length is in the order of centimeters, which prevents the development of significant Coulomb forces between spacecraft and complicates the use of the Electrostatic Tractor in LEO. However, in the hot and tenuous GEO environment, the Debye length is at least 180–200 meters for standard solar conditions, allowing for Coulomb forces in the order of milli-Newtons between spacecraft [BWHS18].

Previous research investigated the charged relative motion dynamics and control of the ET for two spherical spacecraft, and how charge uncertainty affects the control stability [HS13]. If the charge uncertainty exceeds a critical value, the closed-loop relative motion control bifurcates and causes the two spacecraft to collide. However, given the symmetric shape and charge distribution of a single sphere, attitude effects were not studied in prior work. The Multi-Sphere Method (MSM), which uses several spheres to represent complex shapes, approximates electrostatic forces between charged bodies with little computational effort [SS13b, HS19]. This enables the consideration of complex spacecraft shapes and the resulting forces for research on charged astrodynamics.

The focus of this work is to investigate the effects of electrostatic potential uncertainty on the equilibria of the relative motion control for complex three-dimensional shapes using MSM. It is assumed that both spacecraft are fully conducting, and that only the debris potential is estimated inaccurately while the potential of the servicing satellite is perfectly known. Section 2 reviews the relative motion dynamics and control as described in Reference [HS13] and gives an introduction to the Surface MSM model. The effects of electrostatic potential errors are examined in Section 3. First, the equilibria under normal conditions are studied, i.e., for a specific separation distance and spacecraft orientation. Then, the change of the equilibrium solutions for varying separation distances is considered. Finally, the effects of spacecraft attitude are investigated. Section 4 compares the performance of different MSM models with various numbers of spheres.

2. DYNAMICS MODEL

2.1. Relative Motion Dynamics

The relative motion dynamics are derived in Reference [HS13] and are revisited here for convenience. A Hill frame $\mathcal{H} : \{\hat{\boldsymbol{h}}_r, \hat{\boldsymbol{h}}_\theta, \hat{\boldsymbol{h}}_h\}$ with origin at the tug's center of mass is defined by

$$\hat{\boldsymbol{h}}_r = \frac{\boldsymbol{r}_T}{r_T}, \quad \hat{\boldsymbol{h}}_\theta = \hat{\boldsymbol{h}}_h \times \hat{\boldsymbol{h}}_r, \quad \hat{\boldsymbol{h}}_h = \frac{\boldsymbol{r}_T \times \dot{\boldsymbol{r}}_T}{|\boldsymbol{r}_T \times \dot{\boldsymbol{r}}_T|} \tag{1}$$

where $\boldsymbol{r}_T$ is the inertial position vector of the tug, $\dot{\boldsymbol{r}}_T$ is the inertial velocity vector, and $r_T = |\boldsymbol{r}_T|$. The position of the debris is described with the relative position vector $\boldsymbol{\rho}$:

$$\boldsymbol{r}_D = \boldsymbol{r}_T + \boldsymbol{\rho} \tag{2}$$

Solving for $\boldsymbol{\rho}$

$$\boldsymbol{\rho} = \boldsymbol{r}_D - \boldsymbol{r}_T \tag{3}$$

and taking two inertial time derivatives gives

$$\ddot{\boldsymbol{\rho}} = \ddot{\boldsymbol{r}}_D - \ddot{\boldsymbol{r}}_T. \tag{4}$$

The inertial acceleration of the tug is

$$\ddot{\boldsymbol{r}}_T = -\frac{\mu}{r_T^3}\boldsymbol{r}_T + \frac{\boldsymbol{F}_c}{m_T} + \boldsymbol{u}_T \tag{5}$$

where $\mu = 6.674 \times 10^{-11}$ m^3 kg^{-1} s^{-2} is the gravitational constant and m_T is the mass of the servicing satellite. The first term in Eq. (5) corresponds to the gravitational acceleration, $\boldsymbol{F}_c$ is the electrostatic force acting on the tug due to the charged debris, and $\boldsymbol{u}_T$ is the thruster control acceleration generated by the tug's inertial thrusters to perform a low-thrust semimajor axis orbit change. Similarly, the inertial acceleration of the debris is

$$\ddot{\boldsymbol{r}}_D = -\frac{\mu}{r_D^3}\boldsymbol{r}_D - \frac{\boldsymbol{F}_c}{m_D} \tag{6}$$

with the mass of the debris m_D. Substituting Eqs. (5) and (6) into Eq. (4) yields the relative Equations of Motion (EOM):

$$\ddot{\boldsymbol{\rho}} = -\frac{\mu}{r_D^3}\boldsymbol{r}_D + \frac{\mu}{r_T^3}\boldsymbol{r}_T - \frac{\boldsymbol{F}_c}{m_D} - \frac{\boldsymbol{F}_c}{m_T} - \boldsymbol{u}_T \tag{7}$$

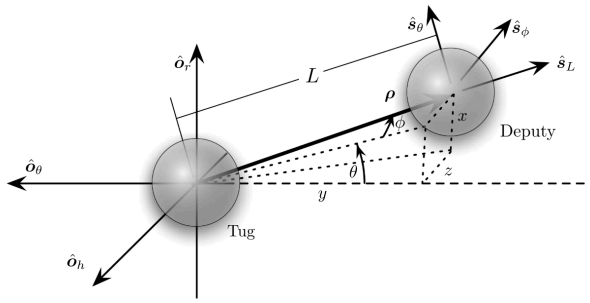

Figure 2: Hill frame $\mathcal{H}$ and Spherical frame $\mathcal{S}$ [HS13]

Combining the thruster control acceleration $\boldsymbol{u}_T$ and the electrostatic force $\boldsymbol{F}_c$ to the total control acceleration vector

$$\boldsymbol{u} = -\boldsymbol{F}_c \left(\frac{1}{m_T} + \frac{1}{m_D} \right) - \boldsymbol{u}_T \tag{8}$$

brings the EOM to a form that is equivalent to the Clohessy-Wiltshire-Hill (CWH) relative motion EOM:

$$\ddot{\boldsymbol{\rho}} = -\frac{\mu}{r_D^3}\boldsymbol{r}_D + \frac{\mu}{r_T^3}\boldsymbol{r}_T + \boldsymbol{u} \tag{9}$$

The linearized form of Eq. (9) is obtained using the relative position vector expressed in the Hill frame ${}^{\mathcal{H}}\boldsymbol{\rho} = [x, y, z]^T$:

$$\ddot{x} - 2n(t)\dot{y} - 3n^2(t)x = u_x \tag{10a}$$
$$\ddot{y} + 2n(t)\dot{x} = u_y \tag{10b}$$
$$\ddot{z} + n^2(t)z = u_z \tag{10c}$$

Because a semi-major axis orbit change is performed, the mean motion $n = \sqrt{\mu/a^3}$, with semimajor axis a, is not constant but a function of time, $n = n(t)$. The electrostatic force is in the order of milli-Newtons and requires low thrust in the same range. Thus, the orbit angular acceleration $\dot{n}$ is in the order of n^3 and is neglected [HS13].

The cartesian form of the EOM in Eq. (10) is not convenient for control design because the equations are coupled. A spherical frame $\mathcal{S} : \{\hat{\boldsymbol{s}}_L, \hat{\boldsymbol{s}}_\theta, \hat{\boldsymbol{s}}_\phi\}$ is introduced with separation distance L between the tug and debris, in-plane rotation angle θ, and out-of-plane rotation angle ϕ, as illustrated in Figure 2. The angles θ and ϕ are a 3-2 Euler angle rotation sequence with respect to the Hill frame $\mathcal{H}$. The direction cosine matrix (DCM) that maps from $\mathcal{H}$ to $\mathcal{S}$ is:

$$[SH] = \begin{bmatrix} \cos\phi\sin\theta & -\cos\phi\cos\theta & -\sin\phi \\ \cos\theta & \sin\theta & 0 \\ \sin\theta\sin\phi & -\cos\theta\sin\phi & \cos\phi \end{bmatrix} \tag{11}$$

The relations between the Hill frame and spherical frame coordinates are

$$L = \sqrt{x^2 + y^2 + z^2} \tag{12a}$$
$$\theta = \arctan\left(\frac{x}{-y}\right) \tag{12b}$$
$$\phi = \arcsin\left(\frac{-z}{L}\right) \tag{12c}$$

and

$$\begin{bmatrix} x \\ y \\ z \end{bmatrix} = [SH]^T \begin{bmatrix} L \\ 0 \\ 0 \end{bmatrix} = \begin{bmatrix} L\sin\theta\cos\phi \\ -L\cos\theta\cos\phi \\ -L\sin\phi \end{bmatrix}. \tag{13}$$

Taking the time derivative of Eq. (13) twice and substituting into Eq. (10) yields the spherical relative equations of motion:

$$\begin{bmatrix} \ddot{L} \\ \ddot{\theta} \\ \ddot{\phi} \end{bmatrix} = [\boldsymbol{F}(L, \theta, \phi, \dot{L}, \dot{\theta}, \dot{\phi})] + [G(L, \phi)]\, {}^{\mathcal{S}}\boldsymbol{u} \tag{14}$$

with

$${}^{\mathcal{S}}\boldsymbol{u} = \begin{bmatrix} u_L \\ u_\theta \\ u_\phi \end{bmatrix}, \tag{15}$$

$$[\boldsymbol{F}] = \begin{bmatrix} \frac{1}{4}L\Big(n^2\left(-6\cos(2\theta)\cos^2\phi + 5\cos(2\phi) + 1\right) \\ \qquad \Big(3n^2\sin\theta\cos\theta + 2\dot{\phi}\tan\phi\big(n + \dot{\theta}\big)\Big) \\ \frac{1}{4}\sin(2\phi)\left(n^2\big(3\cos(2\theta) - 5\big) - 2\dot{\theta}\big(2n + \dot{\theta}\big)\right) \\ \qquad +4\dot{\theta}\cos^2\phi\big(2n + \dot{\theta}\big) + 4\dot{\phi}^2\Big) \\ \qquad -2\frac{\dot{L}}{L}\big(n + \dot{\theta}\big) \\ \qquad -2\frac{\dot{L}}{L}\dot{\phi} \end{bmatrix}, \tag{16}$$

and

$$[G] = \begin{bmatrix} 1 & 0 & 0 \\ 0 & \frac{1}{L\cos\phi} & 0 \\ 0 & 0 & -\frac{1}{L} \end{bmatrix}. \tag{17}$$

2.2. Relative Motion Control Design

A globally asymptotically stabilizing feedback-control is developed in Reference [HS13]

$${}^{\mathcal{S}}\boldsymbol{u} = [G(L, \phi)]^{-1}\Big(- [P]\dot{\boldsymbol{X}} - [K](\boldsymbol{X} - \boldsymbol{X}_r) - [\boldsymbol{F}(L, \theta, \phi, \dot{L}, \dot{\theta}, \dot{\phi})]\Big) \tag{18}$$

where $\boldsymbol{X} = [L, \theta, \phi]^T$, $\boldsymbol{X}_r$ includes the desired steady-state values L_r, θ_r, ϕ_r, and $[K]$ and $[P]$ are positive definite gain matrices. As in Eq. (8), the total control acceleration ${}^{\mathcal{S}}\boldsymbol{u}$ includes both the electrostatic force and the acceleration by the thrusters:

$${}^{\mathcal{S}}\boldsymbol{u} = -{}^{\mathcal{S}}\boldsymbol{F}_c \left(\frac{1}{m_T} + \frac{1}{m_D} \right) - {}^{\mathcal{S}}\boldsymbol{u}_T \tag{19}$$

Using Eq. (18) to obtain ${}^{\mathcal{S}}\boldsymbol{u}$, the required thruster control acceleration is computed by

$${}^{\mathcal{S}}\boldsymbol{u}_T = -{}^{\mathcal{S}}\boldsymbol{u} - {}^{\mathcal{S}}\boldsymbol{F}_c \left(\frac{1}{m_T} + \frac{1}{m_D} \right). \tag{20}$$

The thruster acceleration consists of a feedback term ${}^{\mathcal{S}}\boldsymbol{u}$ and a feed-forward term of the electrostatic force $\boldsymbol{F}_c$. Uncertainty in the estimation of the electrostatic potential of debris results in an inaccurate prediction of the Coulomb force. This motivates the analysis of the electrostatic potential uncertainty effects on the Electrostatic Tractor relative motion control.

2.3. Multi-Sphere Method

The electrostatic potential V of an isolated object in vacuum is related to the charge q

$$V = \frac{q}{C} \tag{21}$$

where C is the object's capacitance. If another object is in proximity, the charge on both objects changes due to mutual capacitance effects. For two spheres with radii R_1, R_2, potentials V_1, V_2, charges q_1, q_2, and separation distance L, the voltage to charge relationship changes to [JS11]:

$$\begin{bmatrix} V_1 \\ V_2 \end{bmatrix} = k_c \begin{bmatrix} 1/R_1 & 1/L \\ 1/L & 1/R_2 \end{bmatrix} \begin{bmatrix} q_1 \\ q_2 \end{bmatrix} \tag{22}$$

If the potentials on both spheres are constant, Eq. (22) is inverted to obtain the charges of the spheres. Knowing the charges q_1 and q_2, the electrostatic force is computed with Coulomb's law

$$F = k_c \frac{q_1 q_2}{r^2} \tag{23}$$

where $k_c = 8.988 \times 10^9$ N m^2 / C^2 is the Coulomb constant. However, general 3D geometries of a spacecraft and the resulting charge distribution cannot be modeled accurately with a single sphere. Additionally, single sphere models are unable to account for torques that result from two spacecraft with complex shapes. The Multi-Sphere Method (MSM) uses a number of spheres to represent general spacecraft geometries and to approximate the charge distribution of the objects [SS13b, HS19]. Knowing the charge on each sphere, the forces and torques between multiple bodies are computed accurately and faster-than-realtime. For multiple spheres, the voltage to charge relationship is

$$\begin{bmatrix} V_1 \\ V_2 \\ \vdots \\ V_n \end{bmatrix} = k_c \begin{bmatrix} 1/R_1 & 1/r_{1,2} & \cdots & 1/r_{1,n} \\ 1/r_{2,1} & 1/R_2 & \cdots & 1/r_{2,n} \\ \vdots & \vdots & \ddots & \vdots \\ 1/r_{n,1} & 1/r_{n,2} & \cdots & 1/R_n \end{bmatrix} \begin{bmatrix} Q_1 \\ Q_2 \\ \vdots \\ Q_n \end{bmatrix} \tag{24}$$

or

$$\boldsymbol{V} = [S]\boldsymbol{Q} \tag{25}$$

with the potential of the i-th sphere V_i, charge Q_i, sphere radius R_i, the vector $\boldsymbol{r}_{i,j}$ from the j-th to the i-th sphere, $r_{i,j} = |\boldsymbol{r}_{i,j}|$, and the elastance matrix $[S]$. Knowing the potentials V_i, Eq. (24) is inverted to obtain the charge of each sphere. For two charged bodies that consist of multiple spheres, Eq. (24) has the form

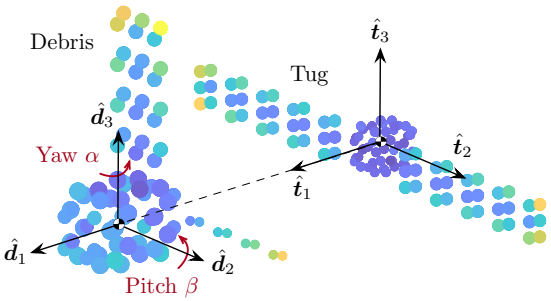

Figure 3: MSM spacecraft models: yellow spheres denote high charge, dark blue spheres represent low charge

$$\begin{bmatrix} \boldsymbol{V}_1 \\ \boldsymbol{V}_2 \end{bmatrix} = \begin{bmatrix} S_1 & S_M \\ S_M^T & S_2 \end{bmatrix} \begin{bmatrix} \boldsymbol{Q}_1 \\ \boldsymbol{Q}_2 \end{bmatrix} \tag{26}$$

where S_M is the mutual capacitance block of the elastance matrix, which changes with the relative position of the two bodies. The diagonal blocks S_1 and S_2 remain constant and do not have to be updated for rigid bodies [MWHS20, WS20b]. Once the charge of each sphere is obtained, the resulting force and torque about point 0 acting on body 1 are computed using

$$\boldsymbol{F}_1 = -k_c \sum_{j=1}^{n_1} \boldsymbol{Q}_{1_j} \left(\sum_{i=1}^{n_2} \frac{\boldsymbol{Q}_{2_i}}{r_{i,j}^3} \boldsymbol{r}_{i,j} \right) \tag{27}$$

and

$$\boldsymbol{L}_{1,0} = -k_c \sum_{j=1}^{n_1} \boldsymbol{r}_j \times \boldsymbol{Q}_{1_j} \left(\sum_{i=1}^{n_2} \frac{\boldsymbol{Q}_{2_i}}{r_{i,j}^3} \boldsymbol{r}_{i,j} \right) \tag{28}$$

where $\boldsymbol{r}_j$ is the vector from point 0 to the j-th sphere.

2.4. Spacecraft Models

Figure 3 shows the MSM models used in this work. The left spacecraft resembles a GOES-R satellite and functions as the debris. It was chosen for this analysis due to its general, asymmetric shape that results from the single solar panel and the magnetometer. The GOES-R bus is modeled as a 4 × 4 × 6 m cuboid, the solar panel has dimensions of 5 × 10 m, and the magnetometer is about 10 m long. The servicing satellite on the right is based on a 2.5 × 2.5 × 3 m SSL-1300 satellite bus with two 3 × 14 m solar panels.

The setup shown in Figure 3 represents the standard (or nominal) configuration. In this configuration, the spacecraft center of mass locations are 20 m apart in the $\hat{\boldsymbol{s}}_L$ direction, and the axes of the debris frame $\mathcal{D} : \{\hat{\boldsymbol{d}}_1, \hat{\boldsymbol{d}}_2, \hat{\boldsymbol{d}}_3\}$ align with the corresponding axes of the tug frame $\mathcal{T} : \{\hat{\boldsymbol{t}}_1, \hat{\boldsymbol{t}}_2, \hat{\boldsymbol{t}}_3\}$.

3. EFFECTS OF ELECTRIC POTENTIAL UNCERTAINTY ON EQUILIBRIUM LOCATIONS

3.1. Sensing the Electrostatic Potential

The relative motion control requires knowledge of the electrostatic force between the two spacecraft. This force depends on the charge distribution of the two bodies, which in turn depends on the electrostatic potentials. Thus, an accurate determination of the potentials is necessary for a desired control behavior. Since the advantage of the Electrostatic Tractor over other ADR methods is that it does not require any physical contact, remote electrostatic potential sensing techniques are essential to keep this ADR method fundamentally touchless.

The Electron Method [BHS19] and the X-ray Method [WS19] provide two promising ways of touchlessly determining the potential of a neighboring satellite. Both methods utilize an active electron beam that is directed at the debris, generating secondary electrons and x-rays. The low-energy secondary electrons are accelerated by the negatively charged debris and arrive at the servicing satellite with a kinetic energy that is equal to the electrostatic potential difference between the two spacecraft. The excited x-ray photons have an energy up to the landing energy of the electrons that are emitted by the electron beam. The difference between the initial energy of the electrons (i.e., the beam energy) and the landing energy (the kinetic energy of the electrons when they impact the debris) corresponds to the electrostatic potential difference between the two craft. Thus, knowing the electron beam energy and the potential of the servicing satellite, the potential of the debris is inferred. Recent progress in remote potential sensing also shows that it is possible to estimate the potential of a neighboring satellite without an active electron beam, using the x-rays that are excited by the ambient plasma environment [WS20a].

However, even tough these remote sensing methods provide means to touchlessly measure the electrostatic potential of the debris, the estimation might be off by a few percent [BWS20, WBS20]. It is important to know how this uncertainty affects the closed-loop response of the relative motion control.

3.2. Equilibria under standard conditions

If the gain matrices $[K]$ and $[P]$ are selected to be orthogonal, the spherical relative EOM in Eq. (14) decouple as

$$\ddot{L} + P_L \dot{L} + K_L(L - L_r) = 0 \tag{29a}$$

$$\ddot{\theta} + P_\theta \dot{\theta} + K_\theta(\theta - \theta_r) = 0 \tag{29b}$$

$$\ddot{\phi} + P_\phi \dot{\phi} + K_\phi(\phi - \phi_r) = 0 \tag{29c}$$

which allows for better analysis of the closed-loop response. If the potential of the debris is estimated, the first equation becomes

$$\ddot{L} + P_L \dot{L} + K_L(L - L_r) = (F_c - F_{c,\text{est}}) \left(\frac{1}{m_T} + \frac{1}{m_D} \right) \tag{30}$$

where $F_{c,\text{est}}$ is the Coulomb force according to the estimated potential and F_c is the actual Coulomb force. Both $F_{c,\text{est}}$ and F_c are the $\hat{\boldsymbol{s}}_L$ components of the electrostatic force vectors $\boldsymbol{F}_{c,\text{est}}$ and $\boldsymbol{F}_c$. Defining

$$\mu_{TD} = \left(\frac{1}{m_T} + \frac{1}{m_D} \right), \tag{31}$$

yields a compact form for the equilibrium solutions of the closed-loop response:

$$K_L(L - L_r) = (F_c - F_{c,\text{est}})\mu_{TD}. \tag{32}$$

Note that, for constant tug and debris potentials V_T and V_D, the actual force $F_c = F_c(L)$ depends on the separation distance L between the tug and the debris. Assuming perfect knowledge of the tug potential V_T, the estimated force $F_{c,\text{est}} = F_{c,\text{est}}(L, \Delta V)$ is a function of L and the estimation error of the debris potential

$$\Delta V = \frac{V_D - V_{D,\text{est}}}{V_D} \tag{33}$$

where V_D is the actual potential and $V_{D,\text{est}}$ is the estimated potential of the debris. Thus, Eq. (32) is rewritten as

$$K_L(L - L_r) - \Big(F_c(L) - F_{c,\text{est}}(L, \Delta V) \Big) \mu_{TD} = 0 \tag{34}$$

where the forces are computed using MSM. The feedback gain K_L must be chosen to compute the equilibrium solutions of Eq. (34). Reference [HS13] shows that

$$K_L \geq \frac{27 \mu_{TD} k_c |\Delta Q|}{4 L_r^3} \tag{35}$$

is required to ensure that positive equilibrium solutions of L exist for the two-sphere model. This formulation considers a charge estimation error

$$\Delta Q = q_T q_D - q_{T,\text{est}} q_{D,\text{est}} \tag{36}$$

instead of an electrostatic potential estimation error ΔV. In the equation above, q_T and q_D are the charges of the tug and the debris, and $q_{T,\text{est}}$ and $q_{D,\text{est}}$ are the estimated charges. Comparing Eq. (35) to Eq. (23) shows that the term $k_c|\Delta Q|/L_r^2$ corresponds to the difference between the actual force and the estimated force:

$$K_L \geq \frac{27 \mu_{TD}}{4 L_r} \Big| F_c(L_r) - F_{c,\text{est}}(L_r, \Delta V) \Big| \tag{37}$$

The required minimal gain K_L depends on the expected potential uncertainty ΔV and the desired reference separation distance L_r. The feedback gain is obtained by substituting the maximum expected potential error ΔV_{max}:

$$K_L = \frac{27 \mu_{TD}}{4 L_{r,KL}} \Big| F_c(L_{r,KL}) - F_{c,\text{est}}(L_{r,KL}, \Delta V_{\text{max}}) \Big| \tag{38}$$

Table 1: Parameters used in this analysis

m_T	m_D	V_T	V_D	$\Delta V_{\max}$
2000 kg	2857 kg	25 kV	-25 kV	10 %

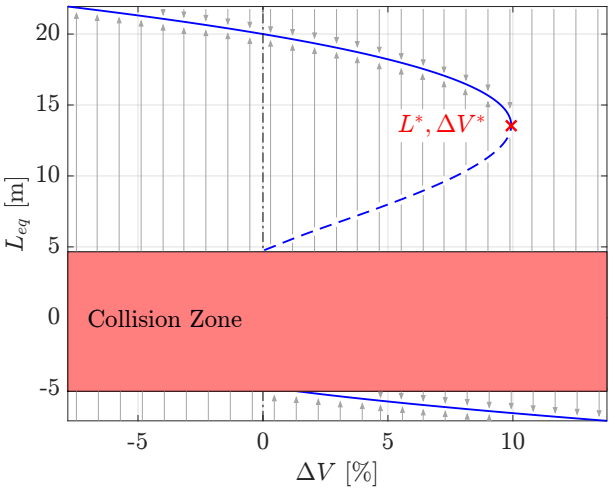

Figure 4: Equilibrium locations L_{eq} of the closed-loop response for potential estimation error ΔV and $L_r = 20$ m: the solid lines correspond to stable equilibria, the dashed line represents unstable equilibria.

Note that L_r was replaced by $L_{r,KL}$ to distinguish between the desired distance L_r and the configuration distance $L_{r,KL}$ that is used to compute the gain, as these two values sometimes differ in the following sections. Equation (34) is solved numerically for the standard spacecraft orientation as shown in Figure 3, using the parameters given in Table 1 and $L_r = 20$ m. The resulting equilibrium locations L_{eq} are shown in Figure 4.

If the electrostatic potential of the debris is underestimated ($\Delta V < 0$), the estimated negative debris potential $V_{D,\text{est}}$ increases in magnitude. Thus, the force is over-predicted and the relative motion control settles to an equilibrium separation distance that is greater than the desired distance L_r. If the debris potential is overestimated ($\Delta V > 0$), the magnitude of the estimated potential $V_{D,\text{est}}$ decreases, and the resulting force is under-predicted. In this case, either two positive and one negative equilibrium solutions exist or only one negative solution, depending on the error ΔV. The underestimation of the electrostatic force pulls the servicing satellite closer to the debris. Only one of the positive equilibria is stable, depicted by the solid line in the the figure, while the other positive equilibrium solution is unstable and represented by a dashed line. The arrows in Figure 4 illustrate the domain of attraction.

The closed-loop response bifurcates at the critical point $(L^*, \Delta V^*)$. A potential error that is greater than the critical error ΔV^* results in one negative root. As the relative motion control settles towards this negative equilibrium location, the servicing satellite would have to pass through the debris, causing a collision. The separation distances where the two spacecraft geometries intersect are represented by the shaded region in Figure 4 and labeled as the Collision Zone. An equilibrium location that is within this region, or a negative equilibrium solution, causes the two spacecraft two collide. Thus, an estimation error that is greater than the critical error ΔV^* must be avoided as it would cause a collision. Note that the critical error is approximately equal to the expected maximum estimation error, which is 10 % in this analysis, if the feedback gain is computed using Eq. (38).

The location of the critical point can also be approximated by replacing the complex spacecraft models with effective spheres. Reference [HS13] shows that

$$L^* = \frac{2}{3} L_r \tag{39}$$

for a two-sphere model. While this relation is exact for the two-sphere model, it only holds approximately for general 3D geometries. The charge estimation error at this distance is:

$$\Delta Q^* = -\frac{4 K_L L_r^3}{27 k_c \mu_{TD}} \tag{40}$$

This critical value is also obtained with Eq. (36):

$$\Delta Q^* = q_T q_D - q^*_{T,\text{est}} q^*_{D,\text{est}} \tag{41}$$

The charges q_T and q_D correspond to the actual spacecraft potentials V_T and V_D, while $q^*_{T,\text{est}}$ and $q^*_{D,\text{est}}$ result from the critical potential estimation error ΔV^*. Assuming perfect knowledge of the tug potential, the charges are determined by inverting Eq. (22):

$$q_T = \frac{L^*(L^* R_T V_T - R_T R_D V_D)}{k_c(L^{*2} - R_T R_D)} \tag{42a}$$

$$q_D = \frac{L^*(L^* R_D V_D - R_T R_D V_T)}{k_c(L^{*2} - R_T R_D)} \tag{42b}$$

$$q^*_{T,\text{est}} = \frac{L^*(L^* R_T V_T - R_T R_D V_D(1 + \Delta V^*))}{k_c(L^{*2} - R_T R_D)} \tag{42c}$$

$$q^*_{D,\text{est}} = \frac{L^*(L^* R_D V_D(1 + \Delta V^*) - R_T R_D V_T)}{k_c(L^{*2} - R_T R_D)} \tag{42d}$$

Substituting Eq. (42) into Eq. (41) gives

$$\Delta Q^* = \frac{L^{*2} R_T R_D}{k_c^2 (L^{*2} - R_T R_D)^2} \cdot \left[L^* R_D \Delta V^{*2} + \right. \\ \left. + \left(2 L^* R_D V_D - (L^{*2} + R_T R_D) V_T\right) \Delta V^* \right] \tag{43}$$

This expression depends on the radii of the effective spheres R_T and R_D. The self-capacitance of a sphere is given by

$$C = 4\pi\varepsilon_0 R = \frac{R}{k_c} \tag{44}$$

where ε_0 is the vacuum permittivity. Since the self capacitance of the spacecraft is known from the MSM models, the effective sphere radii are approximated by:

$$R_T = C_T k_c \qquad R_D = C_D k_c \tag{45}$$

Equating Eq. (40) with Eq. (43) and using Eq. (39) yields the quadratic formula

$$\Delta V^{*2} + b\Delta V^* + c = 0 \tag{46}$$

where

$$b = 2 - \frac{3}{2L_r R_D}(\frac{4}{9}L_r^2 + R_T R_D)\frac{V_T}{V_D} \tag{47a}$$

$$c = \frac{K_L k_c(\frac{4}{9}L_r^2 - R_T R_D)^2}{2R_T R_D^2 \mu_{TD} V_D^2} \tag{47b}$$

The solution of Eq. (46) is

$$\Delta V_{1,2}^* = -\frac{b}{2} \pm \sqrt{\frac{b^2}{4} - c} \tag{48}$$

Examining the terms in Eq. (47) shows that only the minus sign in front of the square root yields a reasonable solution. The equation above is only exact for two spheres with known radii, but provides an approximation of the critical error for two complex shaped spacecraft that are replaced by two effective spheres:

$$\Delta V^* \approx -\frac{b}{2} - \sqrt{\frac{b^2}{4} - c} \tag{49}$$

3.3. Change over distance

It is interesting to see how the closed-loop response is affected by changes to the reference spacecraft separation distance L_r. This analysis considers two cases:

- Case 1: Changes to the reference distance L_r without adjustment of the feedback gain K_L
- Case 2: Changes to the reference distance L_r with a feedback gain K_L that is adjusted to the new reference distance

Equation (38) shows that the gain K_L is configured for a certain reference distance $L_{r,KL}$. Thus, it is expected that the closed-loop response changes if the desired distance L_r of the controller differs from the configuration distance $L_{r,KL}$. While one would not intentionally change the reference distance without adjusting the feedback gain, this can happen for other reasons. For example, erroneous relative position measurements essentially change the reference distance L_r: if the servicer tries to maintain a separation distance of 20 m and the sensors estimate a relative distance of 20 m, even though the spacecraft are just 15 m apart in reality, then $L_r = 15$ m instead of the expected 20 m.

The effects of changes to the reference distance without adjustment of the feedback gain (Case 1) are shown in Figure 5 for a configuration distance of $L_{r,KL} = 20$ m. If $L_r = L_{r,KL}$, the critical potential estimation error is approximately equal to the maximum expected error,

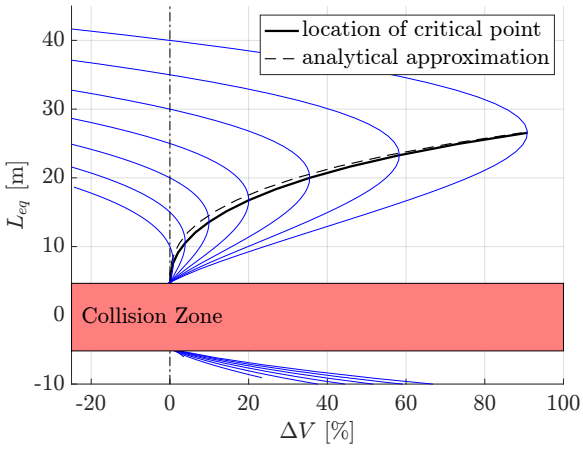

Figure 5: Changes to the reference distance L_r without adjustment of the gain K_L, for $L_{r,KL} = 20$ m

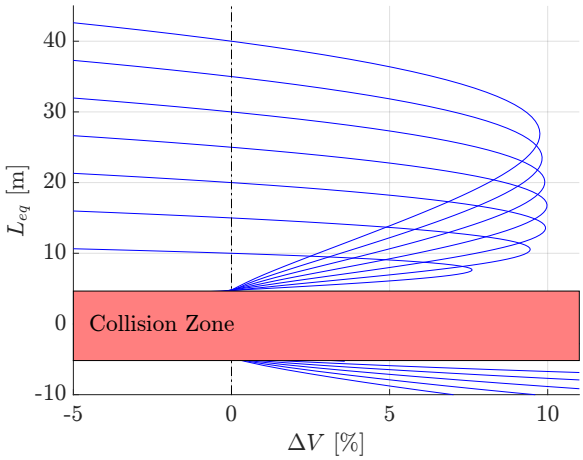

Figure 6: Changes to the reference distance L_r with adjusted feedback gain K_L

$\Delta V^* \approx \Delta V_{\max} = 10$ %, since the controller was set up for this separation distance. The magnitude of the electrostatic force decreases proportional to $1/L^2$, so increasing the reference distance such that $L_r > L_{r,KL}$ results in a larger critical error. Thus, a larger uncertainty of the debris potential can be handled without causing a collision. At some point, the critical error exceeds 100 %. However, if $\Delta V > 100$ %, the estimated debris potential is positive even though the actual potential of the debris is negative, so the controller would expect a repelling force instead of an attractive force. This drastically changes the dynamics of the relative motion control, so estimation errors greater than 100 % are not considered in this analysis. If $L_r < L_{r,KL}$, the critical error decreases, because the electrostatic force is stronger in closer proximity. This means that an estimation error that is smaller than the maximum expected error leads to a collision of the spacecraft.

Figure 5 also displays the location of the critical points, represented by the solid black line, and the corresponding approximation according to Eq. (49), denoted by the

dashed line. For small separation distances, where the electrostatic forces are strong and the difference between the two-sphere model and the MSM model are of greater importance, the approximation deviates from the actual locations. However, for greater distances, the locations are approximated remarkably well.

Figure 6 shows how changes to the reference distance affect the equilibrium locations if the feedback gain is adjusted for each value of L_r. Since the gain K_L, according to Eq. (38), is set up such that the critical error approximately equals the maximum expected error, $\Delta V^* \approx 10\ \%$ for each reference distance. However, Eq. (38) is based on a two-sphere model. For small separation distances, the differences between the two-model and the MSM model become more significant, so the critical potential estimation error deviates from the maximum expected error.

3.4. Change over attitude

The implementation of MSM models enables the study of attitude effects on the closed-loop response for generally shaped spacecraft. According to Figure 3, the debris is re-oriented by changing the yaw α and the pitch β, where $-180° < \alpha < 180°$ and $-90° < \beta < 90°$. The yaw axis aligns with the solar panel of the GOES-R satellite, the pitch axis points in the direction of the magnetometer, and the geometric center of the debris serves as the pivot point. This analysis of the attitude effects only considers the case where $\Delta V = \Delta V^*$.

Figure 7 shows how different spacecraft orientations affect the critical estimation error ΔV^*. For the standard orientation $(\alpha = 0°, \beta = 0°)$ that was considered in the previous sections, the critical error is about 10 % if $L_r = L_{r,KL}$. However, this critical error reaches values as low as 2 % for some debris orientations, meaning that a potential estimation error of just 2 % already causes a collision. The green areas correspond to debris orientations that increase the critical error, so a larger estimation error can be tolerated without causing the two satellites to collide. These regions generally correlate with those orientations where both the solar panel and the magnetometer point away from the tug. The blue areas, on the other hand, designate the orientations that decrease the critical error. This poses a risk because the tug would collide with the debris at an estimation error that is smaller than the maximum expected error. The dark blue regions at $(\alpha = 0°, \beta = -90°)$ and $(\alpha = \pm 180°, \beta = 90°)$ correspond to orientations where the solar panel of the debris satellite is directed towards the servicing satellite, and the valley at $\alpha = 90°$ is due to the magnetometer pointing to the servicer.

Essentially, the distance between the center of charge of each spacecraft decreases if one of the debris' features, such as the solar panel or the magnetometer, is directed towards the servicer. In an effective two-sphere model, this corresponds to a scenario where the two spheres are

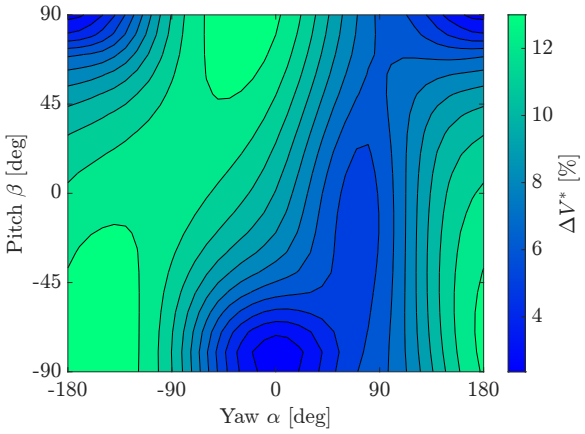

Figure 7: Attitude effects on the critical potential estimation error ΔV^*

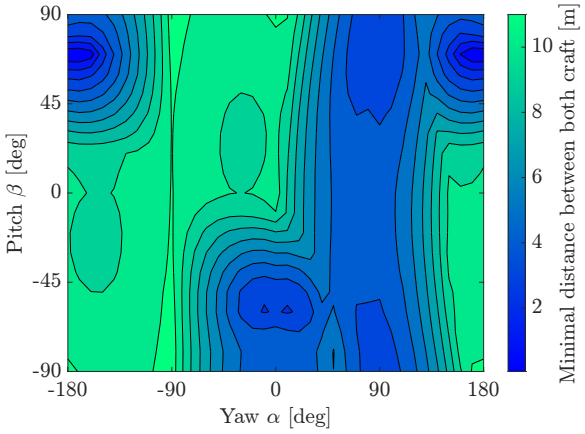

Figure 8: Attitude effects on the minimal distance between the debris and the servicer, for $\Delta V = \Delta V^*$

separated by a distance that is smaller than the reference distance L_r. As shown in the previous section, a smaller reference distance decreases the critical error, and vice-versa, if the feedback gain is not adjusted (Figure 5). For the worst case orientations, where the solar panel is aimed at the servicing satellite, the critical error decreases drastically to only about 2 %, even though the maximum expected estimation error is 10 %. For the best case orientation, however, the critical error increases only marginally to a little over 13 %.

The effects of debris attitude on the minimal distance between both spacecraft in the $\hat{s}_L$ direction is displayed in Figure 8. For each debris orientation, the length of the line connecting the two closest points between the tug and the debris is computed. The long peak at $\alpha = -90°$ and the valley at $\alpha = 90°$ correspond to the magnetometer of the debris pointing away and towards the servicer, respectively, and the dark blue circular regions accord to the orientations where the solar panel is directed towards the tug.

The minimal distance between the debris and the servicer is significantly lower than the reference distance

$L_r = 20$ m due to the following reasons. First, since this attitude analysis is done for an estimation error of $\Delta V = \Delta V^*$, the center-to-center equilibrium separation distance of the two spacecraft is about two thirds of the reference distance, or about 13 m, according to Eq. (39). Second, the reference distance is based on the distance between the center of the debris and the center of the tug, so the size of the spacecraft buses further decreases the minimal space between the two craft by a few meters. In the case where the debris' solar panel or magnetometer – both of which are about 10 m long – is directed towards the servicer, the minimal distance reduces severely to less than 1 meter, despite a reference distance of 20 m.

Note that the regions of low critical error in Figure 7 generally match with the areas of low minimal distance in Figure 8. If one of the debris' features points towards the servicer, induced charging effects move the center of charge of each spacecraft closer to the other one, which decreases the critical estimation error. At the same time, this reduces the minimal distance due to the length of these structures. While intriguing, this offers a clear choice for a worst case scenario, which can be used to select the feedback gain of the relative motion control accordingly. This limits the closest reference distance that can be achieved, unless a control law is implemented that adjusts the separation distance according to the debris orientation.

Figure 9 and Figure 10 show how these attitude effects are affected by changes to the reference distance L_r by looking at the worst and best case scenarios. The worst case orientation is at $(\alpha = 0°, \beta = -90°)$, where the critical error drops to 2.4 %, and the best case orientation is at $(\alpha = -30°, \beta = 90°)$, where the critical error rises to 13.7 %. Like in the previous section, it is differentiated between adjusting the feedback gain for every reference distance, and keeping the same gain across all distances. The nominal orientation corresponds to the scenario shown in Figure 3.

In Figure 9, the feedback gain is not updated. The distance effects dominate the attitude effects, because the critical error increases for both the worst and best case scenario.

Figure 10 displays the attitude effects over distance for the case where the feedback gain is adjusted for every reference distance. The curves from both the worst and best case scenario converge to the critical estimation error of 10 % that corresponds to the standard orientation. The attitude effects are quite significant for distances up to 50 m, and even at 150 m the deviation from the standard critical error is still noteworthy. Note that Debye shielding is neglected in this analysis, which would decrease the impact of electrostatic forces at greater distances, and consequently reduce the attitude effects as well. At a distance over 200 m in GEO, Debye screening essentially prevents the two charged spacecraft from exerting electrostatic forces on each other. However, these results suggest that attitude effects should be considered at any separation distance in a tugging scenario where electrostatic forces are effective.

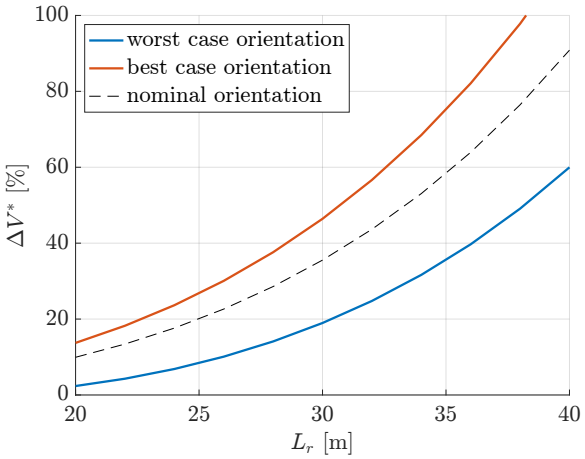

Figure 9: Attitude effects over distance, without adjustment of the gain K_L, for $L_{r,KL} = 20$ m

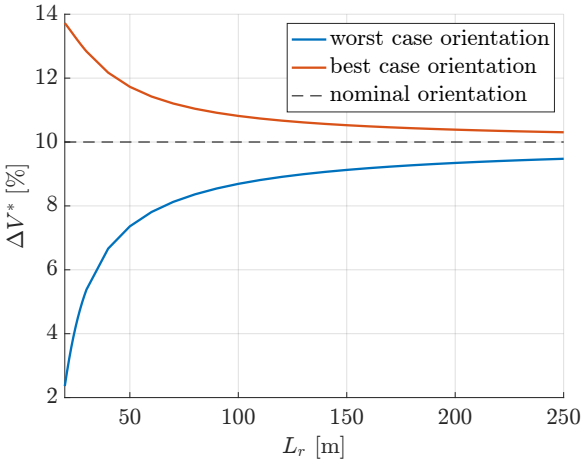

Figure 10: Attitude effects over distance, with adjusted feedback gain K_L

4. MULTI-SPHERE METHOD MODEL COMPARISON

The analysis in the previous sections is based on a debris MSM model with 80 spheres and a servicer model with 108 spheres. However, a large number of spheres increases the computational costs. Thus, the effects of lower-fidelity MSM models are investigated in this section.

For the surface MSM models, the spacecraft surfaces are discretized into triangles, and each sphere of the MSM model is placed at the centroid of a triangle [HS19]. Consequently, at least two spheres are required for a rectangular surface, which limits the minimum number of spheres for the spacecraft MSM models. For example, each spacecraft bus consists of six rectangular sides, so at least $6 \times 2 = 12$ spheres are required for the bus.

Table 2: MSM Model configurations

Configuration ID	Debris			Servicer		
	# of bus spheres	# of feature spheres	total # of spheres	# of bus spheres	# of feature spheres	total # of spheres
A	48	32	80	48	60	108
B	48	18	66	48	32	80
C	48	8	56	48	8	56
D	12	8	20	12	8	20
E	12	4	16	12	4	16
F	-	-	1	-	-	1

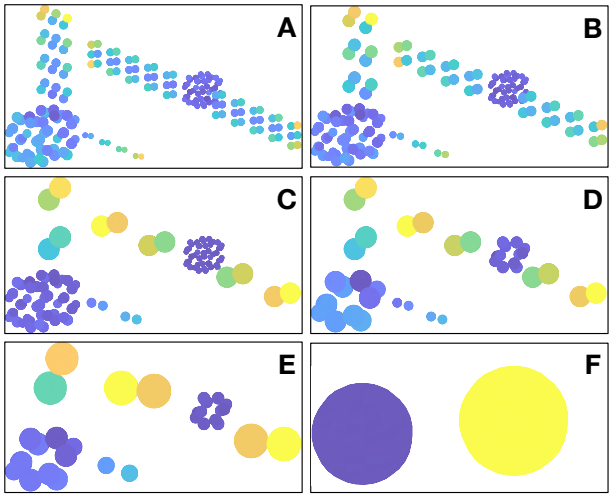

Figure 11: MSM Models

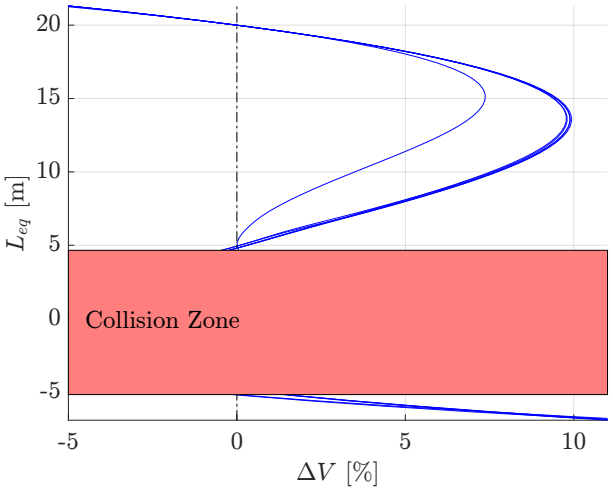

Figure 12: MSM model effects for standard scenario

Figure 11 and Table 2 show the different MSM model configurations that are used in this analysis. The number of feature spheres corresponds to the number of spheres that are used for geometries like the solar panel and magnetometer. For the lowest-fidelity model (Configuration F), a single effective sphere represents the spacecraft, and is placed at the center of charge of the corresponding spacecraft. The center of charge is computed using the Configuration A MSM models in their standard orientations as shown in Figure 3.

4.1. Standard conditions

First, the equilibrium locations are computed for the standard spacecraft orientations and for a reference distance of $L_r = L_{r,KL} = 20$ m (Figure 12). Most of the equilibria curves agree with the highest-fidelity MSM model (Configuration A). Only Configuration F, which consists of one effective sphere placed at the center of charge of each spacecraft, deviates significantly. The deviation of ΔV at the critical point ($L^* = 2/3\ L_r$) corresponds to the difference between the analytical approximation of the critical point and the actual value for $L_r = 20$ m as seen in Figure 5.

4.2. Attitude

Next, the critical estimation error ΔV^* is computed for the worst and best case orientation using the different MSM model configurations. The absolute difference between the computed values and the corresponding values using Configuration A is shown in Figure 13, for each configuration. Note that the critical error is already given in units of %. A difference of +1 %, for instance, means that the lower-fidelity MSM model predicts a critical error of 3 % if the highest-fidelity MSM model yields a value of 2 %. Configuration B and C deviate just slightly from Configuration A. For the worst case orientation, there is almost no difference going from configuration C to D. Even though the number of spheres on the debris decreases from 56 to 20, this change only comes from a reduced number of bus spheres, while the number of feature spheres remains the same. On the other hand, the difference between configuration D and E is significant despite only reducing the total spheres by four, as the number of feature spheres decreases while the modeling of the bus does not change.

The effects of the two sphere effective sphere model (Configuration F) are interesting, as the deviation of the

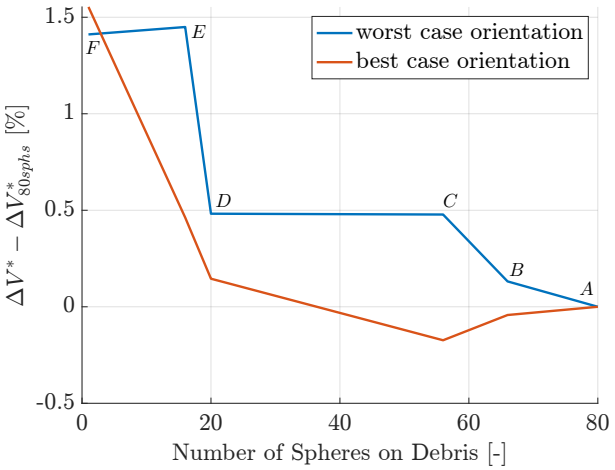

Figure 13: MSM model effects on critical estimation error of worst and best case scenario

best case orientation increases significantly (as expected), while the deviation of the worst case orientation actually decreases with respect to Configuration E. This is due to the following reasons. First, since the effective sphere of the debris is placed at the spacecraft's center of charge, and rotated about the geometric center of the actual spacecraft to represent different debris orientations, some attitudes are represented more accurately than others. The center of charge is computed for the standard orientation of the debris, but varies if the orientation is changed. Second, a single sphere cannot account for any induced charging effects due to the other spacecraft, which generally accumulates charge at the sides of the spacecrafts that face each other. These induced charging effects are even more significant when some of the debris' features point towards the servicing satellite, which is the case for the worst case orientation. Finally, according to Figure 12, the critical error for the standard orientation of Configuration F is already almost 3 % lower than that of the other configurations. Since the critical error is smaller for the worst case orientation, the negative offset of Configuration F at the standard orientation gives the two-sphere model a head start and reduces the ΔV^* deviation.

The results imply that priority must be given to the distribution of spheres on the spacecraft's features – such as solar panels, magnetometers, and other protruding structures – while the spacecraft's bus can be modeled with a minimal number of spheres. Charge accumulates at the edges and corners of conducting objects. For spacecraft, this corresponds to the protruding structures, noticeable in Figure 3. Thus, it is important to accurately model these structures with MSM. The deviations are reasonably small for all models, including Configuration F. However, the strong dependency of the effective sphere model on the location of the center of charge at the standard orientation makes the two-sphere model unfavorable. A center of charge that is located at or near the geometric center of the satellite, which serves as the pivot point for the debris rotations, would prevent any information of the attitude effects.

Table 3: Computation time improvements with respect to Configuration A

Configuration	B	C	D	E	F
# of Spheres	66	56	20	16	1
Improvement [%]	20.0	56.1	83.6	86.8	94.8

4.3. Computation time

Last, the reduction in computation time due to a decrease in the number of spheres is investigated. For this analysis, the data in Figure 7 is computed with each MSM model configuration, and the computation times are compared to that of Configuration A, as seen in Table 3. As expected, the computation time decreases with a reduction in the number of spheres. The effective sphere model is almost twice as fast as Configuration A. However, Configuration D is just slightly slower than Configuration F, at a much higher accuracy according to Figure 12 and Figure 13.

5. CONCLUSIONS

This paper analyzes the effects of electrostatic potential uncertainty on the Electrostatic Tractor (ET) relative motion control for complex spacecraft geometries. If the estimation error of the debris potential exceeds the critical value, the closed-loop response bifurcates and causes the servicing satellite to collide with the debris. The critical value decreases drastically if the debris is oriented in a way that protruding structures such as solar panels are directed towards the servicer, and this attitude also reduces the minimal distance between the two spacecraft significantly, limiting the smallest possible reference separation distance that is used for the controller. Additionally, these consequences of different debris orientations are significant for any reasonable ET separation distance. Thus, attitude effects must be considered when choosing a reference separation distance. One way to mitigate the attitude effects is to select a feedback gain based on the worst case orientation, which generally corresponds to the orientation described above.

Computational effort can be reduced by decreasing the number of spheres that are used for the Multi-Sphere Method spacecraft models. The distribution of spheres should be focused on protruding structures like solar panels, while a spacecraft's bus can consist of a smaller number of spheres. The implementation of effective spheres that are placed at the center of charge of higher fidelity spacecraft models is not recommended due to the dependency on the location of the center of charge, and because the reduction in computational effort is marginal compared to low fidelity Multi-Sphere models.

ACKNOWLEDGMENTS

This work is supported through Air Force Office of Scientific Research grant #FA9550-20-1-0025. The authors would like to thank Kieran Wilson for fruitful discussions.

REFERENCES

AS19. Vladimir Aslanov and Hanspeter Schaub. Detumbling attitude control analysis considering an electrostatic pusher configuration. *Journal of Guidance, Control, and Dynamics*, 42(4):900–909, 2019.

Asl17. Vladimir S. Aslanov. Exact solutions and adiabatic invariants for equations of satellite attitude motion under Coulomb torque. *Nonlinear Dynamics*, 90(4):2545–2556, dec 2017.

AY18. Vladimir Aslanov and Vadim Yudintsev. Motion control of space tug during debris removal by a coulomb force. *Journal of Guidance, Control, and Dynamics*, 41(7):1476–1484, 2018.

BHS19. Miles Bengtson, Joseph Hughes, and Hanspeter Schaub. Prospects and Challenges for Touchless Sensing of Spacecraft Electrostatic Potential Using Electrons. *IEEE Transactions on Plasma Science*, 47(8):3673–3681, aug 2019.

BP11. Claudio Bombardelli and Jesus Peláez. Ion beam shepherd for contactless space debris removal. *Journal of Guidance, Control, and Dynamics*, 34(3):916–920, 2011.

BS15. Trevor Bennett and Hanspeter Schaub. Touchless electrostatic Three-dimensional detumbling of large Axi-symmetric debris. *Journal of the Astronautical Sciences*, 62(3):233–253, 2015.

BWHS18. M Bengtson, K Wilson, J Hughes, and H Schaub. Survey of the electrostatic tractor research for reorbiting passive GEO space objects. *Astrodynamics*, 2(4):291–305, dec 2018.

BWS20. M. T. Bengtson, K. T. Wilson, and Hanspeter Schaub. Experimental Results of Electron Method for Remote Spacecraft Charge Sensing. *Space Weather*, 18(3), may 2020.

DTB15. Roger Dudziak, Sean Tuttle, and Simon Barraclough. Harpoon technology development for the active removal of space debris. *Advances in Space Research*, 56(3):509–527, 2015.

FL17. Stefan Frey and Stun Lemmens. Status of the space environment: Current level of adherence to the space debris mitigation. *JBIS - Journal of the British Interplanetary Society*, 70(2-4):118–124, 2017.

HS13. Erik A. Hogan and Hanspeter Schaub. Relative Motion Control For Two-Spacecraft Electrostatic Orbit Corrections. *Journal of Guidance, Control, and Dynamics*, 36(1):240–249, jan 2013.

HS19. Joseph A Hughes and Hanspeter Schaub. Heterogeneous surface multisphere models using method of moments foundations. *Journal of Spacecraft and Rockets*, 56(4):1259–1266, 2019.

JAH05. R. Jehn, V. Agapov, and C. Hernández. The situation in the geostationary ring. *Advances in Space Research*, 35(7):1318–1327, 2005.

JS11. Lee E Z Jasper and Hanspeter Schaub. Effective Sphere Modeling for Electrostatic Forces on Three-Dimensional Spacecraft Shapes. In *AAS/AIAA Spaceflight Mechanics Meeting*, Girdwood, Alaska, 2011.

KCP78. Donald J Kessler and Burton G. Cour-Palais. Collision frequency of artificial satellites: The creation of a debris belt. *Journal of Geophysical Research*, 83(A6):2637, 1978.

MIB+08. Naomi Murdoch, Dario Izzo, Claudio Bombardelli, Ian Carnelli, Alain Hilgers, and David Rodgers. Electrostatic tractor for near Earth object deflection. *Proc 59th Int Astronautics Conf*, 2008.

MK19. C. Priyant Mark and Surekha Kamath. Review of Active Space Debris Removal Methods. *Space Policy*, 47:194–206, 2019.

MWHS20. Jordan Maxwell, Kieran Wilson, Joseph Hughes, and Hanspeter Schaub. Multisphere method for flexible conducting space objects: Modeling and experiments. *Journal of Spacecraft and Rockets*, 57(2):225–234, 2020.

NK11. Shin Ichiro Nishida and Satomi Kawamoto. Strategy for capturing of a tumbling space debris. *Acta Astronautica*, 68(1-2):113–120, 2011.

NKO+09. Shin Ichiro Nishida, Satomi Kawamoto, Yasushi Okawa, Fuyuto Terui, and Shoji Kitamura. Space debris removal system using a small satellite. *Acta Astronautica*, 65(1-2):95–102, 2009.

PKM09. P. Papushev, Yu Karavaev, and M. Mishina. Investigations of the evolution of optical characteristics and dynamics of proper rotation of uncontrolled geostationary artificial satellites. *Advances in Space Research*, 43(9):1416–1422, 2009.

SGG16. Minghe Shan, Jian Guo, and Eberhard Gill. Review and comparison of active space debris capturing and removal methods. *Progress in Aerospace Sciences*, 80:18–32, 2016.

SGG17. Minghe Shan, Jian Guo, and Eberhard Gill. Deployment dynamics of tethered-net for

space debris removal. *Acta Astronautica*, 132(October 2016):293–302, 2017.

SM12. Hanspeter Schaub and Daniel F. Moorer. Geosynchronous large debris reorbiter: Challenges and prospects. *Journal of the Astronautical Sciences*, 59(1-2):165–180, 2012.

ŠPHS18. Jiří Šilha, Jean Noël Pittet, Michal Hamara, and Thomas Schildknecht. Apparent rotation properties of space debris extracted from photometric measurements. *Advances in Space Research*, 61(3):844–861, 2018.

SS13a. Hanspeter Schaub and Daan Stevenson. Prospects of relative attitude control using coulomb actuation. *Advances in the Astronautical Sciences*, 147(2013):119–135, 2013.

SS13b. Daan Stevenson and Hanspeter Schaub. Multi-Sphere Method for modeling spacecraft electrostatic forces and torques. *Advances in Space Research*, 51(1):10–20, 2013.

WBS20. K. T. Wilson, M. T. Bengtson, and H. Schaub. X-ray Spectroscopic Determination of Electrostatic Potential and Material Composition for Spacecraft: Experimental Results. *Space Weather*, 18(4):1–10, 2020.

WS19. Kieran Wilson and Hanspeter Schaub. X-Ray Spectroscopy for Electrostatic Potential and Material Determination of Space Objects. *IEEE Transactions on Plasma Science*, 47(8):3858–3866, aug 2019.

WS20a. Kieran T. H. Wilson and Hanspeter Schaub. Environmental x-ray considerations for bremsstrahlung-based surface potential determination. In *AIAA SciTech*, Orlando, Florida, jan 2020.

WS20b. Kieran T. H. Wilson and Hanspeter Schaub. Impact Of Electrostatic Perturbations On Proximity Operations In High Earth Orbits. In *AAS/AIAA Astrodynamics Specialist Conference*, Lake Tahoe, CA, aug 2020.

Yak05. M. Yakovlev. The "IADC Space Debris Mitigation Guidelines" and supporting documents. In *4th European Conference on Space Debris*, volume 587, pages 591–597, Darmstadt, Germany, 2005.